2024 IEEE/ASME International Conference on Advanced Intelligent Mechatronics (AIM)
July 15-19, 2024. Boston, MA, USA

Design and Gait Optimization of an In-Pipe Robot with Bistable Inflatable Fabric Actuators

Weijia Tao, Fuchen Chen, Ying Xu, Andrew Johnson, and Wenlong Zhang*

Abstract— **Pipe inspection robots are critical for detecting leaks or cracks, especially in environments that are harmful or inaccessible to humans. In particular, sewage pipes pose significant challenges for traditional rigid pipe robots because they can be filled with obstacles and liquid. Soft robots have been proposed to address some of the issues, but they are still limited in their ability to negotiate obstacles. In this paper, we propose a novel pipe inspection robot powered by a new class of bistable inflatable fabric actuators (BIFA). The entire robot weighs only 350 grams and can exert around 35 N of force by firmly anchoring to the pipe. It is also able to operate in pipes that are blocked by up to 34%. To understand the dynamics of the robot and simulate it for gait optimization, a reduced-order model is proposed and calibrated with characterization experiments including static loading, step response, and anchor test. A Central Pattern Generator (CPG) is also employed to parameterize the gait, enabling Bayesian Optimization in simulation to maximize the robot's speed inside an unobstructed pipe. The optimized gait from the optimization is directly deployable on the real robot and results in a 120% speed increase over the baseline at 23 mm/s, showing the effectiveness of our model and the importance of gait selection for pipe robots.**

I. Introduction

Utility pipes are crucial in maintaining public health and environmental safety, making it important to conduct regular inspections of these critical infrastructures. Currently, these pipes are mostly inspected by human operators, which is often less safe, time-consuming, and prone to inaccuracy and limited accessibility. To address these limitations, in-pipe robots are increasingly deployed to identify blockages, leaks, and structural damages. Various pipe inspection robots that consist of rigid components have been developed and can be classified based on their locomotion type: track [1], inchworm [2], screw [3], walking [4], wheel [5] and gauge [6]. These rigid robots share many advantages such as high speed, precision, and power, but they are also expensive, heavy, difficult to waterproof, and prone to getting stuck in the mud or other obstacles inside the pipe.

On the other hand, soft robots have emerged as promising alternatives for pipe inspection because of their low cost, mechanical compliance, and ease of waterproofing. Soft silicone rubber actuators have been used to build robots that employ inchworm-type locomotion to travel in straight or curved pipes and even climb vertically [7], [8]. Similarly, fabric-based pneumatic actuators have also been employed to build an inchworm-inspired soft robot with even more compliance [9]. Moreover, an inspection robot for sub-centimeter tubular environments is made possible through dielectric elastomer actuators [10].

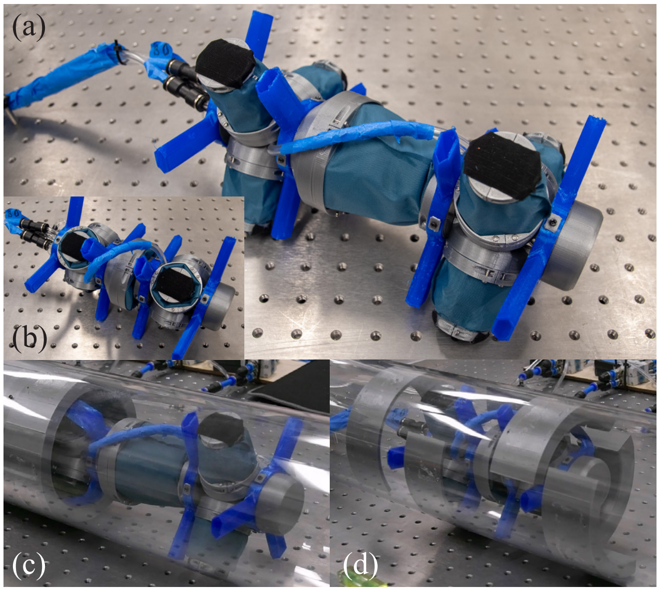

Fig. 1. (a) The proposed pipe inspection robot. (b) The robot is in its fully contracted state. (c) The robot moves through a pipe with a smaller tunnel. (d) The robot demonstrates compliance with different obstacles. A supplementary video is also available at `https://youtu.be/V_8gGbeBEn0`.

However, none of the aforementioned robots have demonstrated the capability to pass through obstacles or narrow tunnels in the pipes, which is a critical requirement for pipe inspection robots. For example, water supply pipes may introduce partial blockage by mineral buildup from hard water, rust in older metal pipes, or sediment and water sewage pipes may be partially blocked by tree roots, trash, and rocks. One notable exception is a soft robot with anchoring chambers that can change their radius significantly [11]. It can go through pipes with diameters from 26 to 51 mm, but at a relatively slow speed of roughly 1.9 mm/s or 0.02 body lengths per second (BL/s), according to the figures in the paper. Additionally, the paper only demonstrates scenarios where the pipe diameter changes are smooth and less frequent.

To address the gap in the literature, this work proposes an

This material is based upon work supported in part by the National Science Foundation under Grant No. 2222816, and in part by Salt River Project.

W. Tao, F. Chen, and W. Zhang are with the School of Manufacturing Systems and Networks, Ira A. Fulton Schools of Engineering, Arizona State University, Mesa, AZ, 85212, USA. Email: {`wtao11, fchen65, wenlong.zhang`}`@asu.edu`.

Y. Xu and A. Johnson are with Water Engineering Support, Salt River Project, Phoenix, AZ, 85072, USA. Email: {`ying.xu, andy.johnson`}`@srpnet.com`.

* Address all correspondence to this author.

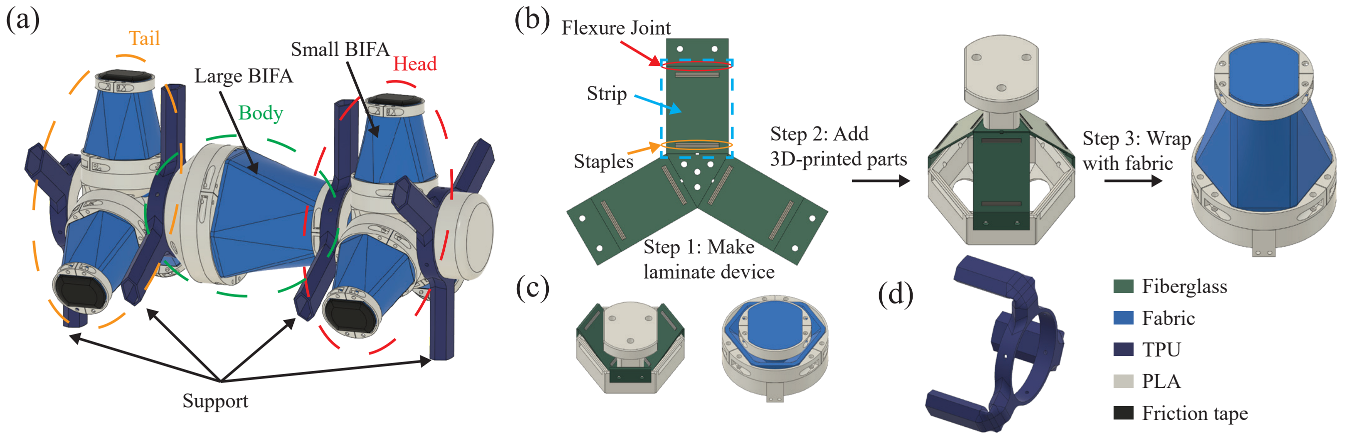

Fig. 2. Design and fabrication of the robot. (a) The head, body, tail, and supports of the robot. (b) Key steps for fabricating BIFA. (c) The contracted BIFA with and without the fabric pouch. (d) The buckled supports.

in-pipe robot, as shown in Fig. 1, that travels at a relatively fast speed and has a high level of mechanical compliance to pass through different obstacles. The robot is equipped with novel bistable inflatable fabric actuators (BIFAs) with large linear deformation ranges and high force output. It also has flexible supports that will passively buckle and conform to obstacles. To improve the robot's speed, a Central Pattern Generator (CPG) [12] is also employed to parameterize the gait for optimization without obstacles. Lastly, the robot is lightweight and low-cost. Its BIFAs not only allow the robot to anchor in the pipe without energy consumption and pressurization but also allow for compact packing during transportation.

In summary, the contributions of this paper are:

- A novel in-pipe robot design powered by BIFAs for passing through obstacles,
- A reduced-order model of BIFAs and the entire robot, along with detailed experiments and analysis of their characteristics, and
- A successful experimental demonstration of a CPG-based gait optimizer to improve the robot speed with directly deployable gait parameters optimized by simulations.

The remainder of the paper is organized as follows: Section II details the design and fabrication of the robot. Section III introduces the modeling of the actuator and the robot, followed by characterization experiments and system identification in Section IV. With the identified robot model, Section V explains the approach for gait generation and optimization for overall robot speed. Experiment results of the comparisons between the baseline and optimized gait are presented and discussed in Section VI. Finally, Section VII concludes the paper and points out some future directions.

II. DESIGN AND FABRICATION

Our final prototype robot weighs around 350 g and measures 240 mm long when extended. It is designed to go through narrow spaces in pipes with diameters varying from 97 mm (∼4 in) to 147 mm (∼6 in). It can move forward and backward with inchworm locomotion. As shown in Fig. 2, the robot has three individually and pneumatically actuated segments: body, tail, and head. Its body segment contains one large BIFA while its head and tail segments each have 3 small BIFAs. This robot also has flexible supports to remain in the center of the pipe during operation. The robot is designed to operate with pneumatic tethers, which simplifies the integration, allowing us to focus more on mechanical designs and gait optimization.

A. Actuator

As shown in Fig. 2(b), the BIFA has three main components: a flexible laminate device, a fabric pouch, and a 3D-printed connecting structure.

The laminate device consists of five layers of materials. The top and bottom layers are fiberglass sheets (ACP Composites, G-10/FR4 0.45 mm and 0.27 mm), the center layer is a polyethylene terephthalate (PET) sheet (Grafix, Clear Dura-La 0.18 mm), and there are two adhesive layers (Drytac, MHA 0.015 mm) that bond them together. It follows the same design and fabrication method used in our previous work [13], [14]. Each layer is individually laser cut and laminated together with a heat press. Then, a final cut is performed to release the device from its support materials. As shown in step 1 in Fig. 2(b), the laminate device has three main strips connected with flexure joints that behave like hinges and the other end of each strip has another flexure joint, which are all reinforced with staples to prevent delamination.

When fixed onto the 3D printed base, shown in step 2 in Fig. 2(b) and (c), the laminate device is folded into a tetrahedron-like shape and it can either point outward or inward, which are the two stable states: contracted and extended states, of the actuator. Since all the main strips are mostly single-layer, thin, and flexible, a force along the axial direction will deform the laminate device and switch it to the other state. During the transition, energy is first stored inside the bent strips and then quickly released after the equilibrium point.

To actively switch between the two stable states with a pneumatic fabric actuator, a heat-sealable 200 Denier Oxford nylon fabric sheet (Rockywoods, SAM6607) is laser cut and sealed with an impulse sealer (ULINE, H-86) into a pocket, where the laminate device along with the base is inserted into. Then, a tube fitting (McMaster-Carr, 5463K53) is installed onto the fabric with a metal-bounded sealing washer (McMaster-Carr, 93786A100) and nut, after which the pocket is sealed off. Finally, 3D-printed rings with ridges that match the grooves on the base wrap around the two ends of the fabric pouch and lock it, as shown in step 3 of Fig. 2 (b). In this way, a positive pressure inside the pouch will push the laminate device from the contracted to the extended state. Similarly, negative pressure can pull the device back. The triggering pressure depends on the stiffness of the laminate strips and the cross-section area [15], [16].

Two variants of the BIFAs are designed for the body, head, and tail, as shown in 2(a). The dimensions of the two actuators are chosen based on the goal that they should provide a large travel range (more than 40% contraction ratio) while not bent over the breaking point during the transition. The width of the strip is also kept wide so that it can store more energy and a strong enough hinge can be added. While the large actuator uses two 0.45 mm fiberglass layers, one of the layers of the small actuator is 0.27 mm instead for better bending and therefore travel range. Some friction tape is also added to the proximal end of the small actuators also shown in Fig. 2(a).

B. Support

The proposed support has a tube-like structure with a hexagon cross-section and is 3D printed with flexible thermoplastic polyurethane (TPU) material. This structure will buckle when a relatively small force is applied, after which it behaves like two links connected by a hinge joint with small torsional stiffness [17]. In this way, when the robot needs to squeeze through a narrow tunnel, it only needs to overcome the buckling force of the supports and a small friction force inside the tunnel. When coming out of the tunnel, the supports will bounce back to their initial shape and make sure the robot is always aligned with the pipe. The stiffness behavior of the supports is important for the fluent operation of the robot. If the supports are too stiff, the robot has to use more force and energy to bend them. On the other hand, supports that are too soft will fail to keep the robot aligned, affecting both locomotion speed and obstacle negotiation capability. The width, height, and wall thickness of the support are tuned through trial and error.

C. Control System

A control system is built to actuate the robot and collect sensory data. The pneumatic subsystem takes both positive and negative pressure and outputs three binary pressures that are individually addressable. The positive pressure is provided by the building and goes through an electro-pneumatic regulator (SMC, ITV1050-21N2CL4). The negative pressure comes from a vacuum pump (Agilent, DS 202) and no regulator is installed. For each output, 2 solenoid valves (Festo, MHE3-MS1H-3/2G-1/8-K) are used to switch between positive and negative pressure. A pressure sensor (Honeywell, ABPDRRV015PDAA5) that can read both positive and negative pressure is also added to each output near the valves and away from the robot, which greatly simplifies the wiring. The tubes from the valves to the robot are 1/8 in inner diameter (ID) and 1/4 in in outer diameter (OD) and are about 1 m long. Most other tubes have an ID of 3/16 in and OD of 5/16 in except the ones to the pressure sensors, which have an ID of 1/16 in and an OD of 1/8 in. The main electronics of the system include MOSFETs driving the valves, a DAC (Adafruit, MCP4725) for the regulator, a microcontroller (Arduino, Uno) handling the low-level logic, and a laptop issuing commands and collecting data. The data rate is at around 100 Hz.

III. MODELING

To better understand the characteristics and dynamics of the robot and simulate it for efficient gait optimization, this section explains the dynamic model of a single BIFA and its extension to describe the full robot dynamics.

A. Actuator

In this work, a reduced-order model is proposed to describe the dynamic behaviors of a single BIFA. A BIFA can be modeled as two masses connected with a bistable spring, a damper, and a force generator in parallel. The bistable spring has a sine-wave-like force versus displacement curve [18]. The damping mainly comes from the air movement inside the actuator, along with some from the spring. The force generator represents the major force applied to the actuator by air pressure. The dynamics for one of the masses are then described with the following equations:

$$m\ddot{x} = -K(x) - b\dot{x} + F - mg\,, \tag{1}$$

$$\dot{F} = \alpha(p^d a - F)\,, \tag{2}$$

$$\alpha = \begin{cases} \alpha_s, & x > x_{th} \text{ and } p^d < 0 \\ \alpha_n, & \text{otherwise} \end{cases}\,, \tag{3}$$

where x represents the displacement of the mass, K is a polynomial function that outputs force given displacement; b is the damping constant; and g is the gravity acceleration that can be set to zero if the actuator is laying horizontally. Since the exact pneumatic dynamics is complex and depends on many factors such as the compressor characteristics, tube length and diameter, and air chamber volume and shape, a first-order model (2) with a convergence factor α is used to model the rising and dropping of pneumatic forces when a pressure p_d is applied, which is converted to force through a nominal cross-section area a. Furthermore, it is observed that when the actuator is extended and a positive pressure is applied, the fabric will tend to bulge outward and form a ring around the actuator. When a negative pressure is applied under this condition, the pressure inside has to go through a slower drop first, and hence the two different α values and the threshold value x_{th}, as shown in (3). x_{th} is set to the unstable equilibrium point of the bistable spring as marked in

Figs. 4, after which the actuator begins to contract and fold the fabric and there is very little bulge. Lastly, the pressure inside the actuator is estimated as $p = (F - b\dot{x})/a$, which is the pressure-related forces divided by the area.

B. Robot

Since the robot's motion is mostly along the axial direction of the pipe and its body is a single large BIFA, the actuator model with additional friction is proposed to simulate the entire robot. The two masses now each represent a half of the robot which includes the head or tail and a half of the body. The friction applied to each mass mostly depends on normal force against the pipe exerted by the head or tail actuators. In this way, the equations of motion for the head mass are:

$$m_h\ddot{x}_h = -K_b(x_h - x_t) - b_b(\dot{x}_h - \dot{x}_t) + F_b - F_h^f\,, \tag{4}$$

$$F_h^f = \begin{cases} sign(\dot{x}_h)\mu_k N_h, & |\dot{x}_h| > \epsilon \\ sign(F_h')min(\mu_s N_h, |F_h'|), & \text{otherwise} \end{cases}, \tag{5}$$

$$F_h' = -K_b(x_h - x_t) - b_b(\dot{x}_h - \dot{x}_t) + F_b\,, \tag{6}$$

$$N_h = 3F_h^w + m_h g\,, \tag{7}$$

$$F_h^w = \begin{cases} k_w(x_{ha} - x_w) + b_w\dot{x}_{ha}, & x_{ha} > x_w \\ 0, & \text{otherwise} \end{cases}, \tag{8}$$

Both kinetic and static friction are modeled in F_h^f, which are switched by a small speed threshold ϵ and have different friction coefficients μ_k and μ_s. In addition to the gravity, the other component of the normal force N_h comes from the pipe's wall F_h^w, which is modeled as a spring with k_w and damper with b_w that only activates when the displacement of the proximal end of the head actuator x_{ha} is greater than a threshold x_w that is a few millimeters smaller than the extended length of the head actuator. The constant 3 in (7) is to account for the fact that the actual head and tail segments each have three head actuators, which also means that only one head actuator model with states x_{ha} and $\dot{x}_{ha}$ from (1) is used to model the interactions. The equations of motion for the tail are similar and coupled through the forces from the spring, damper, and force generator.

IV. CHARACTERIZATION

A. Actuator Characterization

1) Static Loading Tests: In order to verify and quantify the stiffness behavior and force output capability of the actuators, static loading tests were performed on both the small and large BIFAs with a universal testing system (Instron, 5944) as shown in Fig. 3(a). The actuator was slowly pulled from its contracted state until fully extended and then pushed back. Three trials were performed for each commanded internal pressure and force and displacement data were recorded at 50 Hz.

These data were used to calibrate the actuator models. A 15th-degree polynomial K from (1) was fit to the force and displacement data of the actuator at 0 psi using the NumPy package. Then, the nominal cross-section area a of the actuator was selected to minimize the error between the stiffness curves after being adjusted by the pressure force pa and p is the average pressure readings from the sensor over that trial that is reported in the legends of Fig. 4.

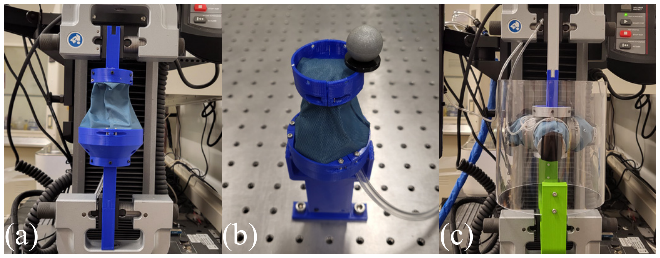

Fig. 3. Characterization experiment setups including: (a) BIFA static loading, (b) BIFA step response, and (c) head anchoring test.

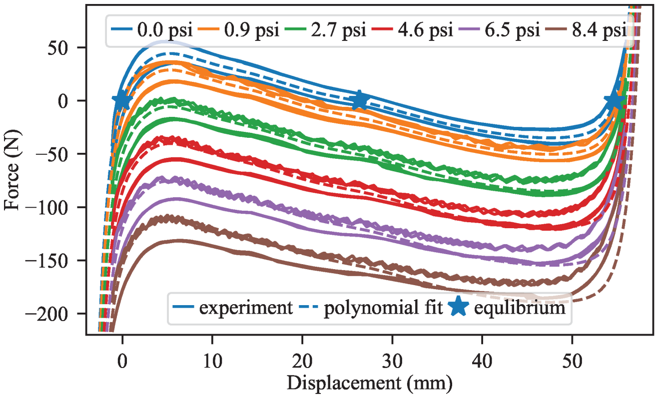

Fig. 4. Stiffness curves of BIFA under different internal pressures.

The experiment data and the polynomial fit of the stiffness curve of the large BIFA under different pressures are plotted in Figs. 4. The force curve is similar to a sine wave as expected. As marked in the figure, the two equilibrium points at the ends represent the two stable states of the bistable mechanism, while the center one is unstable. The curve is also not symmetric both in terms of the distance between the stable and unstable point and the two peak forces, which is mainly due to the nonidealness of the flexure hinge joints. There is also obvious hysteresis.

As the internal pressure increases, the force becomes more negative on average meaning that a larger compression force is needed to hold the actuator in place. The change of forces is also linearly proportional to pressure indicating that the cross-section area is near constant. The curves also demonstrate the large force output capability of the actuators reaching over 150 N in pushing and around 40 N even without the help of pressure for the large BIFA in Fig. 4. The oscillations along the curves are caused by the regulator actively trying to hold the internal pressure constant. The small BIFA shares very similar behavior, and the differences are mostly in force and displacement magnitude and thus omitted.

2) Step Response Tests: Step response tests were also carried out to figure out the dynamic characteristics of the actuators when pressurized. The actuator started from its contracted state with its bigger end mounted on a testing

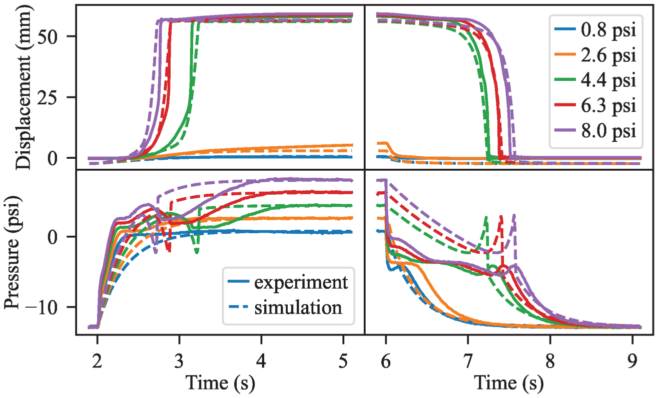

Fig. 5. Extension and contraction step responses of BIFA when different pressures are applied.

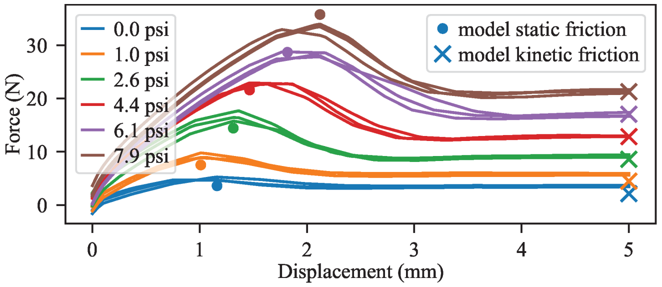

Fig. 6. Anchoring force of the robot head or tail segment.

stand as shown in Fig. 3(b) and a negative pressure applied. Then, a positive pressure was given to the actuator followed by a negative pressure with some time delay. A motion capture system (NaturalPoint, OptiTrack Prime 17W) was used to collect the position data of the smaller end, and the pressure sensor data was also recorded, both with a sampling rate of around 100 Hz. Different positive pressures were commanded and the negative pressure was fixed at full vacuum.

With K and a identified from static loading tests, another optimization was performed to match the transient displacement behavior of our model to the real-world data. The pressure readings from the sensors during the steady states were used for the model simulation, which was numerically solved with LSODA [19] from the SciPy package. The parameters that can be varied were m, b, α_s, and α_n from equations (1) to (3). The optimizer was based on differential evolution [20] from SciPy.

The experimental data and simulation results with the identified model parameters for the step responses of the large BIFA are plotted in Figs. 5. As expected from bistable mechanisms, the actual switching between the two stable states is very fast. Moreover, the proposed actuator model is able to capture the transient behavior well despite a very simple pressure model. The model also overestimates the displacement by about 2 mm under negative pressure and underestimates a similar amount for positive pressure, a result of ignoring the hysteresis with a single polynomial curve. The results for the small BIFA tell a similar story and are omitted.

B. Head/Tail Anchor Characterization

The anchoring capability of the robot was measured by pulling the pressurized head segment from still through a pipe at 20 mm/s and recording the force and displacement data at 50 Hz. Three trials were performed on one sample of the head with different commanded pressures.

Since our model is able to predict the normal force applied to the pipe wall, the maximum force before sliding and the force during sliding from the anchor characterization were used to find the pipe wall threshold x_w in (8), as well as static friction coefficient μ_s and kinetic μ_k friction coefficient in (5), by minimizing the error between model prediction and experimental data.

The results from the anchor characterization are plotted in Fig. 6. When pressurized, one head segment is able to provide up to around 33 N of anchoring force. Even when there is no pressure, one segment can still provide about 5 N which is three times its body gravity if using both the head and tail, making the robot well-suited to anchor both horizontally and vertically and resist disturbances.

V. LOCOMOTION

A. Gait Generation

An open-loop CPG is used to generate the periodic pressure commands for the three segments for efficient locomotion. CPGs are a group of coupled oscillators that generate rhythmic joint trajectories from non-rhythmic inputs [12]. By adjusting the gait parameters such as period, phase offsets, and duty factors, the robot will be able to move forward or backward at various speeds. In this work, the CPG has three oscillators whose phases are coupled through the following equation [14]:

$$\dot{\phi}_i = 2\pi f + \sum_{j=1}^{3} \alpha_\phi c_{ij} sin(\phi_j - \phi_i - \psi_{ij})\,, \tag{9}$$

where f is the gait frequency, $\alpha_\phi = 10$ is a constant controlling the convergence rate, and $\{i, j\} = \{1, 2, 3\}$ which indexes the oscillator for the body, head, and tail segments, respectively. c_{ij} describes the coupling strength between oscillators and $c_{ij} = \begin{cases} 0, \ i = j \\ 1, \ i \neq j \end{cases}$. ψ_{ij} is an element from the matrix ψ which describes the desired phase difference between oscillators as shown below

$$\psi = \begin{bmatrix} 0 & \psi_{12} & \psi_{13} \\ -\psi_{12} & 0 & \psi_{13} - \psi_{12} \\ -\psi_{13} & -(\psi_{13} - \psi_{12}) & 0 \end{bmatrix}.$$

Since the supply pressure is fixed and either a constant positive or negative input pressure is applied to the robot, the phase of each oscillator, wrapped into $[0, 2\pi)$, is converted to a binary output with a duty factor parameter d_i as in $u_i =$

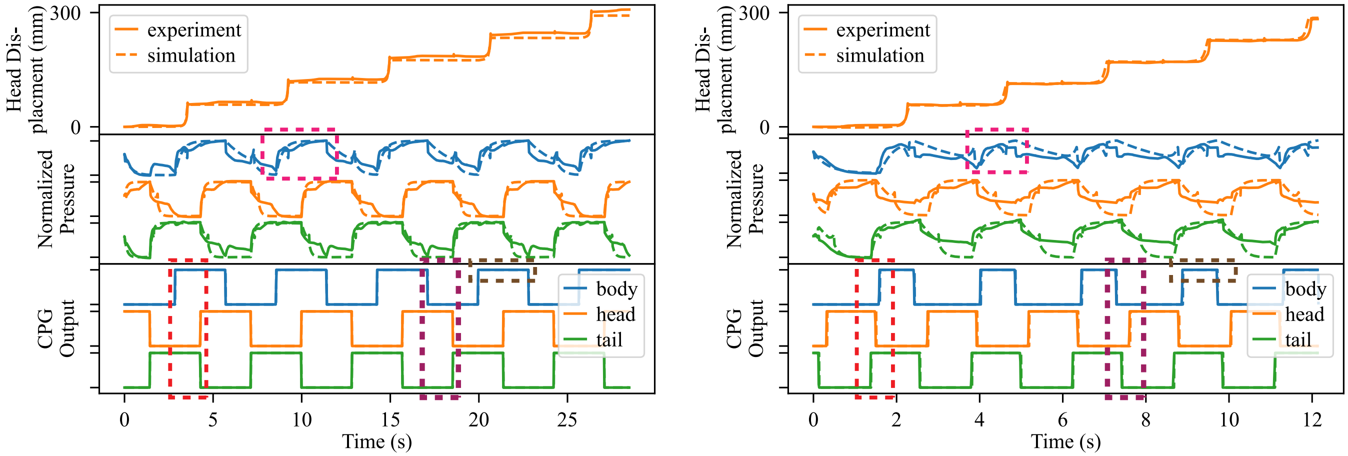

(a) Baseline (b) Optimized

Fig. 7. Comparison between the robot locomotion data and CPG outputs of the (a) baseline and (b) optimized gait.

$\begin{cases} 1, \ \phi_i > 2\pi d_i \\ 0, \ \text{otherwise} \end{cases}$, where an output of 1 means applying positive pressure and 0 means applying negative pressure.

B. *Gait Optimization for Highest Robot Speed*

With the calibrated robot model, a gait optimization that tries to maximize forward speed is conducted on the following CPG parameters: period of a cycle $1/f \in (2, 4)\,s$, phase offset between body and head $\psi_{12} \in (0, 2\pi)$, phase offset between body and tail $\psi_{13} \in (0, 2\pi)$, duty factor of body $d_1 \in (0.2, 0.8)$, and duty factor of head and tail $d_2 = d_3 \in (0.2, 0.8)$. For each trial, the robot is simulated for four cycles and the speed of the final settled cycle is used. It is noticed that the routine tends to find a gait that slips forward, which is hard to reproduce in reality, mainly due to slight misalignment and actuator bending. Therefore, if slipping is detected that is $\dot{x}_h$ and $\dot{x}_t$ are both nonzero, a zero speed is returned. Moreover, a zero will also be returned if a simulation run takes too long to complete. The positive and negative supply pressure in the simulation are -13 psi and 8.5 psi, respectively.

The optimizer is Bayesian Optimization paired with an Upper Confidence Bound acquisition function with $\kappa = 0.5$ favoring exploitation [21]. Three runs with 1000 iterations each are performed with different random seeds. The optimized gait parameters are directly deployed on the real robot for three trials and the head displacement and pressure data are collected at 100 Hz.

For comparison, a baseline gait is also performed both in simulation and experiments where the duty factors are all set to 0.5, the phase differences $\psi_{12} = 1.5\pi$, $\psi_{13} = 0.5\pi$ and the period $1/f = 5.7\,s$ are selected so that the body switches state only when the head or tail fully anchors. We believe that this gait is a reasonable baseline since it can be implemented easily without CPG and requires minimal tuning.

VI. RESULTS AND DISCUSSIONS

A. *CPG-based Gait Optimization*

The results for the baseline and optimized gait from simulation and one trial of the experiment are plotted in Figs. 7(a)-(b). The average speed over five actuation cycles for three trials is 10.8 ± 0.1 mm/s for the baseline and 23.3 ± 0.1 mm/s for the optimized gait, showing a 120% improvement. As shown in the first two rows, the simulation and experimental data match very well, which showcases an effective use of simulation for gait optimization. The small mismatch of the displacement for the baseline gait is likely related to the underestimation of the maximum travel length of the body when the internal pressure reaches a steady state as evident in Fig. 5.

Comparing the plots of the baseline and optimized gait, we identified three main approaches the optimizer used to improve the robot's speed. First, it allocates more time for body contraction than extension with $d_b = 0.66$ compared to $d_b = 0.5$ used in the baseline gait as circled out by the brown box, because the contraction has to deal with the bulging effect of the fabric mentioned previously. Second, since the delay between receiving an extension/contraction command and the actual extension/contraction is longer for the body segment than the head/tail segment as hinted by Fig. 5, it is possible to start the anchoring of the head or tail segment around the same time as the state change command is issued for the body instead of inserting a long wait. This is evident from the CPG output plots where the state switching of the head and tail are closer to the body's for the optimized gait as circled out by the red and purple boxes. Lastly, the internal pressure of the actuators only needs to apply enough force to overcome the peak force of the BIFAs found in Fig. 4 instead of the supply pressure. In the pressure plots, the body pressure for the baseline gait is closer to settling after each transition than the body pressure during the optimized gait as circled out by the magenta box. Comparison of the two gaits can also be found in the supplementary video.

B. Travelling through Obstacles

The robot's ability to travel through obstacles is also demonstrated in Fig. 1(c)-(d) and the supplementary video. The robot's gait for these tasks is similar to the baseline with a slightly longer period $1/f = 6\,\mathrm{s}$, because it is observed that the optimized and baseline gaits both have relatively tight timing not allowing the actuators to fully extend or contract before the next action, resulting in the body not exerting enough force to buckle the supports. With this compromise on speed, the robot is able to successfully move through pipes filled with different types of obstacles: a 50 mm-long tunnel with a diameter of 97 mm (34% blocked compared to the 147 mm original diameter), a 150 mm-long tunnel composed of sub-tunnels with diameters of 137 mm, 97 mm, and 117 mm, and a series of randomly placed arcs with heights of 5 mm, 15 mm, and 25 mm inside the pipe. These results highlight the importance of the robot's mechanical compliance when facing unknown obstacles in pipe inspection.

VII. CONCLUSIONS

This paper presented a novel pipe inspection robot, whose long-travel BIFAs and flexible supports enabled it to move through pipes with obstacles filling up to 34% of the original pipe diameter. Furthermore, the proposed model for the robot, characterization experiments, and the CPG-based gait optimizer allowed us to find the optimal gait parameters for the highest locomotion speed in an unobstructed pipe in simulation, which is 120% faster than the baseline gait when directly deployed into the real system.

Future work will focus on optimizing the robot design, fabrication, and material selections to improve the capability of passing through obstacles, reliability, and travel speed. Modeling and simulation of obstacles to generate a library of gaits for different scenarios are also desirable. Untethered operation and adding sensors for visual feedback are also important steps toward real-world deployment.

ACKNOWLEDGMENT

The authors would like to thank Dr. Daniel M. Aukes and ASU IDEA Lab for providing us access to several essential equipment for this project.

REFERENCES

[1] W. Zhao, L. Zhang, and J. Kim, "Design and Analysis of Independently Adjustable Large In-Pipe Robot for Long-Distance Pipeline," *Applied Sciences*, vol. 10, no. 10, p. 3637, Jan. 2020, number: 10 Publisher: Multidisciplinary Digital Publishing Institute.

[2] D. Chablat, S. Venkateswaran, and F. Boyer, "Mechanical Design Optimization of a Piping Inspection Robot," *Procedia CIRP*, vol. 70, pp. 307–312, Jan. 2018.

[3] A. Nayak and S. K. Pradhan, "Design of a New In-Pipe Inspection Robot," *Procedia Engineering*, vol. 97, pp. 2081–2091, Jan. 2014.

[4] S. Savin, "RRT-based Motion Planning for In-pipe Walking Robots," in *2018 Dynamics of Systems, Mechanisms and Machines (Dynamics)*, Nov. 2018, pp. 1–6.

[5] A. Kakogawa and S. Ma, "Design of amultilink-articulated wheeled pipeline inspection robot using only passive elastic joints," *Advanced Robotics*, vol. 32, no. 1, pp. 37–50, 2018.

[6] D. Mishra, K. K. Agrawal, A. Abbas, R. Srivastava, and R. S. Yadav, "Pig [pipe inspection gauge]: An artificial dustman for cross country pipelines," *Procedia Computer Science*, vol. 152, pp. 333–340, 2019, publisher: Elsevier B.V.

[7] M. S. Verma, A. Ainla, D. Yang, D. Harburg, and G. M. Whitesides, "A Soft Tube-Climbing Robot," *Soft Robotics*, vol. 5, no. 2, pp. 133–137, 2018.

[8] X. Liu, M. Song, Y. Fang, Y. Zhao, and C. Cao, "Worm-Inspired Soft Robots Enable Adaptable Pipeline and Tunnel Inspection," *Advanced Intelligent Systems*, vol. 4, no. 1, p. 2100128, 2022.

[9] W. Adams, S. Sridar, C. M. Thalman, B. Copenhaver, H. Elsaad, and P. Polygerinos, "Water pipe robot utilizing soft inflatable actuators," *2018 IEEE International Conference on Soft Robotics, RoboSoft 2018*, pp. 321–326, 2018, publisher: IEEE ISBN: 9781538645161.

[10] C. Tang, B. Du, S. Jiang, Q. Shao, X. Dong, X.-J. Liu, and H. Zhao, "A pipeline inspection robot for navigating tubular environments in the sub-centimeter scale," *Science Robotics*, vol. 7, no. 66, p. eabm8597, May 2022.

[11] X. Zhang, T. Pan, H. L. Heung, P. W. Y. Chiu, and Z. Li, "A Biomimetic Soft Robot for Inspecting Pipeline with Significant Diameter Variation," *IEEE International Conference on Intelligent Robots and Systems*, pp. 7486–7491, 2018, iSBN: 9781538680940.

[12] A. J. Ijspeert, "Central pattern generators for locomotion control in animals and robots: A review," *Neural Networks*, vol. 21, no. 4, pp. 642–653, May 2008.

[13] F. Chen and D. M. Aukes, "Direct Encoding of Tunable Stiffness Into an Origami-Inspired Jumping Robot Leg," *Journal of Mechanisms and Robotics*, vol. 16, no. 031012, Mar. 2023.

[14] F. Chen, W. Tao, and D. M. Aukes, "Development of A Dynamic Quadruped with Tunable, Compliant Legs," in *2023 IEEE/RSJ International Conference on Intelligent Robots and Systems (IROS)*. Detroit, MI, USA: IEEE, Oct. 2023, pp. 495–502.

[15] W. Tao, Z. Qiao, and W. Zhang, "Design, Characterization, and Dynamic Modeling of BEAST: a Bistable Elastomeric Actuator for Swift Tasks," in *2022 IEEE 5th International Conference on Soft Robotics (RoboSoft)*, Apr. 2022, pp. 390–395.

[16] B. Zhang, "Bistable and multi-stable thin-walled structures," Ph.D. dissertation, University of Oxford, 2017.

[17] Y. Jiang, M. Sharifzadeh, and D. M. Aukes, "Reconfigurable Soft Flexure Hinges via Pinched Tubes," in *2020 IEEE/RSJ International Conference on Intelligent Robots and Systems (IROS)*. Las Vegas, NV, USA: IEEE, Oct. 2020, pp. 8843–8850.

[18] Y. Chi, Y. Li, Y. Zhao, Y. Hong, Y. Tang, and J. Yin, "Bistable and Multistable Actuators for Soft Robots: Structures, Materials, and Functionalities," *Advanced Materials*, vol. 34, no. 19, p. 2110384, May 2022.

[19] A. C. Hindmarsh, "ODEPACK, A Systematized Collection of ODE Solvers," *IMACS Transactions on Scientific Computation*, vol. 1, pp. 55–64, 1983.

[20] R. Storn and K. Price, "Differential Evolution – A Simple and Efficient Heuristic for global Optimization over Continuous Spaces," *Journal of Global Optimization*, vol. 11, no. 4, pp. 341–359, 1997.

[21] F. Nogueira, "Bayesian Optimization: Open source constrained global optimization tool for Python," 2014–.